Time-optimal Control of Electric Race Cars under Thermal Constraints

Locatello, Alessandro

Award date:
2021

Masters Thesis
Automotive Technology

Time-optimal Control of Electric Race Cars under Thermal Constraints

Alessandro Locatello
1382411

Supervisor:

Dr. Ir. Mauro Salazar

Department of Mechanical Engineering
Control Systems Technology
Eindhoven University of Technology (TU/e)
Eindhoven, 5600 MB, The Netherlands
February 2021

TU/e EINDHOVEN UNIVERSITY OF TECHNOLOGY

Declaration concerning the TU/e Code of Scientific Conduct for the Master's thesis

I have read the TU/e Code of Scientific Conduct[i].

I hereby declare that my Master's thesis has been carried out in accordance with the rules of the TU/e Code of Scientific Conduct

Date 29 / 01 / 2021

Name Alessandro Locatello

ID-number 1382411

Signature

Insert this document in your Master Thesis report (2nd page) and submit it on Sharepoint

[i] See: http://www.tue.nl/en/university/about-the-university/integrity/scientific-integrity/
The Netherlands Code of Conduct for Academic Practice of the VSNU can be found here also.
More information about scientific integrity is published on the websites of TU/e and VSNU

Time-optimal Control of Electric Race Cars under Thermal Constraints

Alessandro Locatello
Supervisor: Dr. Ir. Mauro Salazar
Department of Mechanical Engineering, Control Systems Technology
Eindhoven University of Technology (TU/e)
Eindhoven, 5600 MB, The Netherlands
a.locatello@student.tue.nl

***Abstract*— This paper presents a quasi-convex optimization framework to compute the minimum-lap-time control strategies of electric race cars, accurately accounting for the thermal limitations of the Electric Motor (EM). To this end, we leverage a previously developed thermally-unconstrained framework and extend it as follows: First, we identify a thermal network model of an interior permanent magnet EM comprising its shaft, rotor, magnets, stator, windings, and end-windings, including their individual loss-models. Second, we devise a convex battery model capturing the impact of the state of energy on the battery losses. Third, in order to cope with the nonlinearities stemming from the transcription of the problem from time-domain to a position-dependent representation, we leverage an iterative algorithm based on second-order conic programming to efficiently compute the solution. Fourth, we discuss the optimality convergence properties and computational efficiency of the proposed iterative algorithm by solving the problem via nonlinear programming: we observe that the iterative algorithm has a much longer computational time, but it always converges in a predictable time, whilst the inital conditions of the nonlinear solver strongly influence its performance, but when it converges, is guaranteed a locally optimal solution. Finally, we showcase our framework on the Le Mans racetrack. A comparison with high-fidelity simulations in Motor-CAD demonstrate that our proposed model can accurately capture the temperature dynamics of the EM, revealing the end-windings and the magnets to be the limiting components in a cold-start and a long-run operation scenario, respectively. Furthermore, our numerical results underline the considerable impact of the EM thermal dynamics on lap-time, suggesting that using a continuously variable transmission could significantly improve lap-time with respect to a fixed-gear transmission.**

I. Introduction

ELECTRIC racing has been receiving increasing attention over the past decade, for instance, with the emergence of the fully-electric Formula E racing championship and various student electric racing competitions. As in any other class of motorsport, the most important performance indicator is the lap time: the time needed to complete one lap around the race track. Whilst more conventional race cars rely on thermally robust internal combustion engines as their prime mover, electric race vehicles are solely propelled by electric motors (EMs), which are more sensitive to the heating effects during high power operation [1], [2]. Thus, when determining the optimal control strategies of an electric race car, the thermal behavior of the EM has to be accurately accounted for in order to avoid detrimental damages compromising its performance. To this end, this paper presents a quasi-convex modeling and optimization framework to compute the minimum-lap-time control strategies for the battery electric race car shown in Fig. 1, accounting for the thermal strain on the EM. Specifically, the proposed framework allows to accurately characterize the impact of EM heating on the achievable lap time of electric race cars, and to compare the performance achievable with different transmission technologies.

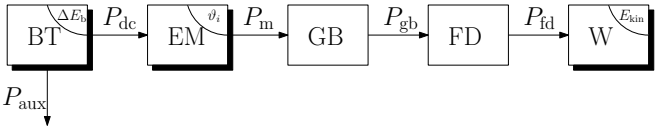

Fig. 1. Schematic layout of the electric powertrain. It consists of a battery pack (BT), an electric motor (EM), a transmission (GB) which is either a fixed-gear transmission (FGT) or a continuously variable transmission (CVT); and a final drive reduction gear (FD) connected to the wheels (W). The arrows indicate the power flows between the components.

Related literature: The problem studied in this paper pertains to two main research areas. The first is devoted to the time-optimal control of (hybrid) electric race cars. A drawback of simultaneously optimizing the velocity profile and the driving trajectory [2], [3] is that the problem becomes highly nonlinear, hence an effective simplification consists of condensing the vehicular dynamics and the expert driver's feeling into a maximum speed profile. This way, the resulting time-optimal energy management problem can be solved with a wide variety of methods, such as convex optimization [4], [5], PMP [6], or a combination of approaches [7], [8]. However, these methods lack accurate thermal models on the component-level, or do not explicitly capture the impact of the transmission on the achievable performance. The second stream of research is devoted to the thermal modeling of electric motors. Typically, this problem is addressed with lumped-parameter thermal networks (LPTNs), computational fluid dynamics (CFD), or finite-element analysis (FEA) [9]. While CFD and FEA can achieve very accurate results at the expense of computational complexity [10], [11], LPTN-based models are the most widely used, as they leverage

equivalent thermal network representations to significantly improve the overall computational tractability [12], [13]. Nonetheless, LPTN-based methods have not yet been applied to racing. In conclusion, to the best of our knowledge, there are no optimization methods to compute the time-optimal control strategies for battery electric race cars, while accurately capturing the temperature dynamics of the EM and characterizing the impact of the transmission on the thermal behavior and overall performance.

Statement of contributions: Against this backdrop, this paper presents an extension of the quasi-convex optimization framework presented in [14] to compute the time-optimal control strategies of a battery electric race car, explicitly accounting for the thermal constraints on the EM and the impact of the transmission technology on the overall performance. In particular, we first derive an almost-convex model of the race car, including an LPTN capturing the temperature dynamics of the EM and a state-of-energy-dependent battery model. Second, we formulate the time-optimal control problem and solve it using an iterative algorithm based on convex programming. Third, we validate our models with the high-fidelity EM simulation software Motor-CAD [15]. Fourth, we showcase our framework with case studies on the Le Mans track, whereby we compare the performance of a fixed-gear transmission (FGT) and a continuously variable transmission (CVT) in cold-start and long-run racing scenarios. A preliminary version of this work has been submitted to the European Control Conference [16]. In this extended version, we underline the time-optimal-control policy regarding regeneration for abundant or scarse battery eneragy availability. Moreover, we discuss the efficiency and effectiveness of the proposed framework by comparing solving time and optimality conditions with a nonlinear solver.

Organization: The remainder of this paper is structured as follows: Section II presents the almost-convex electric powertrain model including an LPTN capturing the EM thermal dynamics, the time-optimal control problem and an iterative algorithm to effectively solve it. We analyze the numerical results stemming from different scenarios in Section III, alongside a validation of the models and a discussion of the optimality and convergence properties of the almost convex iterative algorithm. We draw the conclusions and discuss future research directions in Section IV.

II. Methodology

This section presents an almost-convex model of the race car shown in Fig. 1, frames the time-optimal control problem to be solved by an iterative solution algorithm and a nonlinear solver. The mechanical modeling of the powertrain and the iterative solution approach are inspired by the work presented in [14]. In this paper, we identify and validate a thermal network meticulously characterizing the temperature dynamics of the EM's components and an accurate state-of-energy dependent battery model, which we include in the minimum-lap-time control problem.

As shown in Fig. 1, the battery converts chemical energy to electrical energy which is supplied to the EM. In turn, the EM converts it into mechanical energy and heat losses. The mechanical energy flows through the transmission and the final drive before reaching the wheels, while the losses heat up the EM. In this application, we consider an FGT and a CVT for the transmission. The optimization of the driving path is split from the powertrain control problem, and the characteristics of the track and the vehicular dynamics are condensed into the maximum speed profile $v_{\max}(s)$ as a function of the position on the racetrack s, which can be either measured or pre-computed [4], [5]. For the CVT-equipped vehicle, the input variables are the motor force $F_{\mathrm{m}}(s)$ and the transmission ratio $\gamma(s)$, while we design its maximum ratio $\gamma_{\max}$. For the FGT-equipped vehicle, the transmission ratio γ_1 is a design variable and $F_{\mathrm{m}}(s)$ is the only input. The state variables of the problem are the kinetic energy of the vehicle $E_{\mathrm{kin}}(s)$, the battery state-of-energy $E_{\mathrm{b}}(s)$, and the temperatures of the nodes of the thermal network, specifically—considering an interior permanent magnet EM— of the shaft $\vartheta_{\mathrm{sf}}(s)$, the permanent magnets $\vartheta_{\mathrm{pm}}(s)$, the rotor $\vartheta_{\mathrm{rt}}(s)$, the windings $\vartheta_{\mathrm{wd}}(s)$, the stator $\vartheta_{\mathrm{st}}(s)$, and the end-windings $\vartheta_{\mathrm{ew}}(s)$.

A. Minimum-lap-time Objective

In line with [4], [14], we formulate the time-optimal control problem in space domain, so that it becomes a finite-horizon optimal control problem accommodating position-dependent parameters such as the maximum speed profile. This way, our framework needs to be defined in terms of forces instead of power. The translation to power can be performed in post-processing, using the relation between force and power $F = P/v$ to obtain the power from the optimal solution $P^\star$, using the force $F^\star$ and speed $v^\star$.

Our objective is to minimize the lap time T:

$$\min T = \min \int_0^S \frac{\mathrm{d}t}{\mathrm{d}s}(s)\mathrm{d}s, \tag{1}$$

where S is the length of the track and $\frac{\mathrm{d}t}{\mathrm{d}s}(s)$ is the lethargy, i.e., the inverse of speed $v(s)$. Since speed and lethargy are both optimization variables, it is necessary to establish a convex connection between the variables, defined as

$$\frac{\mathrm{d}t}{\mathrm{d}s}(s) \cdot v(s) \geq 1, \tag{2}$$

which can be written as a second-order conic constraint that will hold with equality at the optimum [4].

B. Longitudinal Vehicle Dynamics

This section presents a convex model of the longitudinal vehicle dynamics in space domain taken from [4], [14]. The kinetic energy is related to speed in a relaxed convex form as

$$E_{\mathrm{kin}}(s) \geq m_{\mathrm{tot}} \cdot v(s)^2/2, \tag{3}$$

where m_{tot} is the total mass of the vehicle. The kinetic energy's dynamics are given by

$$\frac{\mathrm{d}}{\mathrm{d}s}E_{\mathrm{kin}}(s) = F_{\mathrm{p}}(s) - F_{\mathrm{d}}(s), \tag{4}$$

where $F_{\mathrm{p}}(s)$ is the propulsion force and $F_{\mathrm{d}}(s)$ is the drag force. The drag force is defined as

$$F_{\mathrm{d}}(s) = c_{\mathrm{d}} \cdot A_{\mathrm{f}} \cdot \rho \cdot E_{\mathrm{kin}}(s)/m_{\mathrm{tot}} + m_{\mathrm{tot}} \cdot g \cdot (\sin(\alpha(s)) + c_{\mathrm{r}} \cdot \cos(\alpha(s))), \quad (5)$$

where c_{d} is the drag coefficient, A_{f} is the frontal area of the vehicle, ρ is the air density, g is the Earth's gravitational constant, $\alpha(s)$ is the inclination of the track, and c_{r} is the rolling friction coefficient. The propulsive force is modeled in a relaxed convex form as

$$F_{\mathrm{p}}(s) \leq \min\left(\eta_{\mathrm{fd}} \cdot F_{\mathrm{gb}}(s), F_{\mathrm{gb}}(s)/\eta_{\mathrm{fd}}\right), \quad (6)$$

where $F_{\mathrm{gb}}(s)$ is the force on the secondary axle of the transmission. We condense the racetrack characteristics, the vehicular dynamics and the expert driver's feeling into a maximum speed profile, which we enforce as a maximum kinetic energy constraint:

$$E_{\mathrm{kin}}(s) \leq E_{\mathrm{kin,max}}(s) = m_{\mathrm{tot}} \cdot v_{\mathrm{max}}^2(s)/2. \quad (7)$$

Finally, considering a free-flow racing lap, we impose identical speed at the start/finish line as

$$E_{\mathrm{kin}}(0) = E_{\mathrm{kin}}(S). \quad (8)$$

C. Transmission

In this section, we derive a model of the transmission. The speed of the electric motor is expressed by

$$\omega_{\mathrm{m}}(s) = \gamma(s) \cdot \gamma_{\mathrm{fd}}/r_{\mathrm{w}} \cdot v(s), \quad (9)$$

where $\gamma(s)$ is the transmission ratio, γ_{fd} is the fixed final drive transmission ratio, and r_{w} is the radius of the wheels. This constraint is convex if the speed $v(s)$ is given, a property we will leverage throughout this section to devise an iterative convex solver. The transmission ratio is defined as

$$\gamma(s) \begin{cases} = \gamma_1 & \text{if FGT} \\ \in [\gamma_{\min}, \gamma_{\max}] & \text{if CVT,} \end{cases}$$

where $\gamma_1 > 0$ is the ratio of the FGT, and $\gamma_{\min} > 0$ and $\gamma_{\max} > 0$ are the lower and upper limit of the CVT ratio, respectively. Considering $\gamma_{\max}$ as a design variable with a given constant ratio coverage $c_\gamma = \frac{\gamma_{\max}}{\gamma_{\min}} > 1$, we rewrite the constraint above as

$$\gamma(s) \begin{cases} = \gamma_1 & \text{if FGT} \\ \in \left[\frac{\gamma_{\max}}{c_\gamma}, \gamma_{\max}\right] & \text{if CVT.} \end{cases} \quad (10)$$

We assume the transmission efficiency η_{gb} to be constant, and define the force on the secondary axle of the transmission similar to (6):

$$F_{\mathrm{gb}}(s) \leq \min\left(\eta_{\mathrm{gb}} \cdot F_{\mathrm{m}}(s), F_{\mathrm{m}}(s)/\eta_{\mathrm{gb}}\right). \quad (11)$$

D. Electric Motor

In this section, we derive two models of the EM: a speed-independent convex model and a speed-dependent model including a thermal network describing the temperature dynamics of its components. The former model will be instrumental to compute an initial guess of the speed profile, which will be iteratively optimized using the latter model, as presented in more detail in Section II-F below. Furthermore, we solve the nonlinear speed-dependent problem using nonlinear programming. In this case, the first model is used to compute the initial guesses. The nonlinear data that is used to identify and validate the EM model is obtained from the high-fidelity EM simulation software Motor-CAD. We choose a high-performance interior permanent magnet EM among the templates offered by the software. For both speed-independent and -dependent models, we enforce torque and power limits in space-domain as

$$F_{\mathrm{m}}(s) \in \left[-\frac{\gamma(s) \cdot T_{\max}}{r_{\mathrm{w}}}, \frac{\gamma(s) \cdot T_{\max}}{r_{\mathrm{w}}}\right], \quad (12)$$

and

$$F_{\mathrm{m}}(s) \in [-1, 1] \cdot \left(\frac{c_{\mathrm{m},1} \cdot \gamma(s)}{r_{\mathrm{w}}} + c_{\mathrm{m},2} \cdot \frac{\mathrm{d}t}{\mathrm{d}s}(s)\right), \quad (13)$$

where $T_{\max}$, $c_{\mathrm{m},1}$ and $c_{\mathrm{m},2}$ are subject to identification, Appendix A. The limit on the rotational speed of the motor is expressed as

$$\gamma(s) \leq \omega_{\mathrm{m,max}} \cdot r_{\mathrm{w}} \cdot \frac{\mathrm{d}t}{\mathrm{d}s}(s) \cdot \frac{1}{\gamma_{\mathrm{fd}}}, \quad (14)$$

where $\omega_{\mathrm{m,max}}$ is the EM maximum speed.

The EM speed-independent model approximates the losses with a quadratic function as

$$P_{\mathrm{dc}}(s) = \alpha_{\mathrm{m}} \cdot P_{\mathrm{m}}(s)^2 + P_{\mathrm{m}}(s),$$

where $\alpha_{\mathrm{m}} \geq 0$ is an efficiency parameter, subject to identification, Appendix A. We relax the quadratic power approximation and convert it to forces as

$$\frac{\mathrm{d}t}{\mathrm{d}s}(s)\left(F_{\mathrm{dc}}(s) - F_{\mathrm{m}}(s)\right) \geq \alpha_{\mathrm{m}} \cdot F_{\mathrm{m}}(s)^2.$$

This relation can be written as a second-order conic constraint which will hold with equality in the case where the solver converges to a time-optimal solution with limited battery energy [4].

$$\frac{\mathrm{d}t}{\mathrm{d}s}(s) + F_{\mathrm{dc}}(s) - F_{\mathrm{m}}(s) \geq \left\| \begin{matrix} 2 \cdot \sqrt{\alpha_{\mathrm{m}}} \cdot F_{\mathrm{m}}(s) \\ \frac{\mathrm{d}t}{\mathrm{d}s}(s) - F_{\mathrm{dc}}(s) + F_{\mathrm{m}}(s) \end{matrix} \right\|_2, \quad (15)$$

In order to capture the behavior of the EM more accurately, we model it in a speed-dependent fashion. Moreover, we include the thermal dynamics as an LPTN, due to its computational tractability and usability. In contrast to the state of the art [17], where empirical models based on continuous and peak torque operation are used, we explicitly model the temperatures of the EM's individual components. The model is based on the following assumptions: The heat flow in the circumferential direction is neglected, and it is independent in the radial and axial directions. Moreover, we lump the thermal properties of a component into one single node. Fig. 2 shows the Motor-CAD model of the EM and Fig. 3 depicts the thermal network. The EM components under consideration are the shaft (sf), the rotor (rt), the permanent magnets (pm), the stator (st), the windings (wd) and the end-windings (ew), i.e., the overhanging copper cables connecting the windings, which usually represent the most critical component at high-performance operation [18]. Considering the thermal dynamics of the EM, the following

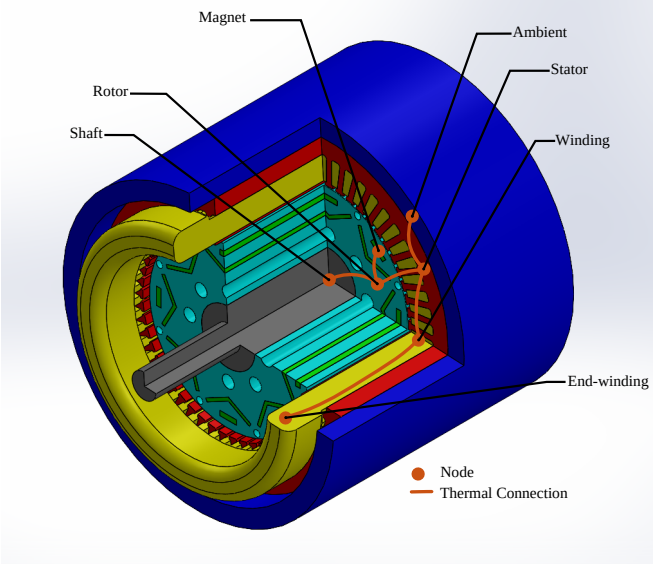

Fig. 2. The Motor-CAD interior permanent magnet motor model with the thermal network. We identify seven main components of the EM. A schematic representation of the thermal network is shown in Fig. 3.

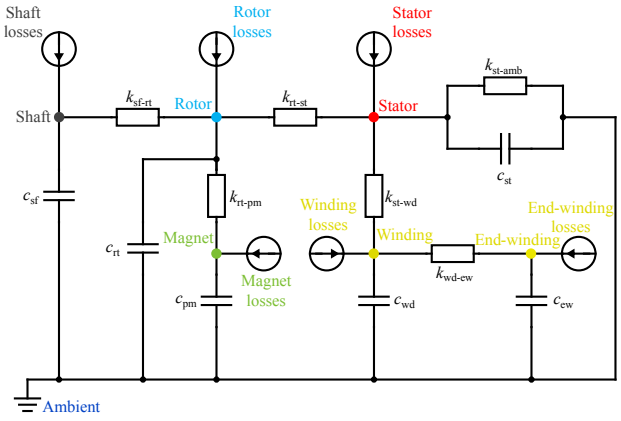

Fig. 3. The thermal network of the motor presented in Fig. 2. Every component of the EM is represented by a node in the thermal network.

energy balance equations describe the heat flows between the components:

$$\begin{cases} P_{\mathrm{sf}} = c_{\mathrm{sf}}\dot{\vartheta}_{\mathrm{sf}} + k_{\mathrm{sf,rt}}(\vartheta_{\mathrm{sf}} - \vartheta_{\mathrm{rt}}) \\ P_{\mathrm{rt}} = c_{\mathrm{rt}}\dot{\vartheta}_{\mathrm{rt}} + k_{\mathrm{sf,rt}}(\vartheta_{\mathrm{rt}} - \vartheta_{\mathrm{sf}}) + k_{\mathrm{rt,pm}}(\vartheta_{\mathrm{rt}} - \vartheta_{\mathrm{pm}}) \\ \qquad + k_{\mathrm{rt,st}}(\vartheta_{\mathrm{rt}} - \vartheta_{\mathrm{st}}) \\ P_{\mathrm{pm}} = c_{\mathrm{pm}}\dot{\vartheta}_{\mathrm{pm}} + k_{\mathrm{rt,pm}}(\vartheta_{\mathrm{pm}} - \vartheta_{\mathrm{rt}}) \\ P_{\mathrm{st}} = c_{\mathrm{st}}\dot{\vartheta}_{\mathrm{st}} + k_{\mathrm{rt,st}}(\vartheta_{\mathrm{st}} - \vartheta_{\mathrm{rt}}) + k_{\mathrm{st,wd}}(\vartheta_{\mathrm{st}} - \vartheta_{\mathrm{wd}}) \\ \qquad + k_{\mathrm{st},\infty}(\vartheta_{\mathrm{st}} - \vartheta_{\infty}) \\ P_{\mathrm{wd}} = c_{\mathrm{wd}}\dot{\vartheta}_{\mathrm{wd}} + k_{\mathrm{st,wd}}(\vartheta_{\mathrm{wd}} - \vartheta_{\mathrm{st}}) + k_{\mathrm{wd,ew}}(\vartheta_{\mathrm{wd}} - \vartheta_{\mathrm{ew}}) \\ P_{\mathrm{ew}} = c_{\mathrm{ew}}\dot{\vartheta}_{\mathrm{ew}} + k_{\mathrm{wd,ew}}(\vartheta_{\mathrm{ew}} - \vartheta_{\mathrm{wd}}), \end{cases}$$

where P_i is the power loss in node i—where the index i indicates the EM component and is an element of the set of strings $\{\mathrm{sf}, \mathrm{rt}, \mathrm{pm}, \mathrm{st}, \mathrm{wd}, \mathrm{ew}\}$—$\vartheta_i$ its temperature, $\dot{\vartheta}_i$ its temperature's rate of change in time domain, c_i its heat capacity, and $k_{i,j}$ represents the overall heat transfer coefficient between two neighboring nodes i and j. Hereby, the coefficients $k_{i,j}$ and c_i are subject to identification.

We estimate the power losses in the individual nodes by fitting a set of experimental data produced by Motor-CAD as a function of speed and mechanical power. We can approximate the nonlinear model in a convex manner using convex quadratic functions. In particular, the losses of the nodes are set equal to $P_i(s) = x_i(s)^\top Q_i x_i(s)$, where Q_i is a symmetric and positive semi-definite matrix, and $x_i(s)$ is defined for each component based on the dependence of its losses on the EM speed and power, and the components' temperature. In order to preserve convexity, the power loss equations are relaxed in the set of constraints

$$P_i(s) \geq x_i(s)^\top Q_i x_i(s). \tag{16}$$

Given the racing application, we expect the motor to operate at high power levels. Therefore, we build a reference EM duty cycle to simulate the power losses in Motor-CAD which we use as fitting data to identify the matrices Q_i. This method allows to minimize the error in the region where the motor is expected to operate. The duty cycle is inspired by the EM operations of the temperature unconstrained problem, Appendix B.

As shown by the reference data in Fig. 4, the mechanical losses are power-independent and only affect the shaft, i.e., $x_{\mathrm{sf}} = \begin{bmatrix} 1 & \omega_{\mathrm{m}}(s) \end{bmatrix}^\top$. Conversely, windings and end-windings are subject to copper losses, which are strongly influenced by the temperature of the components, in addition to the EM speed and power. Therefore, we define $x_i(s) = \begin{bmatrix} 1 & \omega_{\mathrm{m}}(s) & P_{\mathrm{m}}(s) & \vartheta_i(s) \end{bmatrix}^\top$, for $i \in \{\mathrm{wd}, \mathrm{ew}\}$. The permanent magnets and the iron paths of the rotor and stator do not show a relevant thermal dependency and are therefore identified with $x_i(s) = \begin{bmatrix} 1 & \omega_{\mathrm{m}}(s) & P_{\mathrm{m}}(s) \end{bmatrix}^\top$, for $i \in \{\mathrm{pm}, \mathrm{rt}, \mathrm{st}\}$. Similarly, we identify a total loss model dependent on speed and power [14], in order to evaluate the thermally-unconstrained case and compare it with the thermally-constrained scenario. The resulting models are shown in Fig. 4. Appendix C presents the comparison between the power loss data obtained with Motor-CAD and the estimated power loss using the convex quadratic model.

As stated earlier, the coefficients $k_{i,j}$ and c_i of the energy balance equations are subject to identification. We derive these constants using a genetic algorithm as a fitting scheme for the node temperatures over the reference EM duty cycle. Even though we have information about the power loss of each component during the cycle, we use the speed, power, and temperature of the windings and the end-windings to estimate the power losses and identify the thermal network. By doing this, we avoid propagating the error of the power loss model. Overall, the temperature fitting can be observed in Appendix C. The fit root mean square error is below 1 °C.

We convert the set of energy balance equations to space-

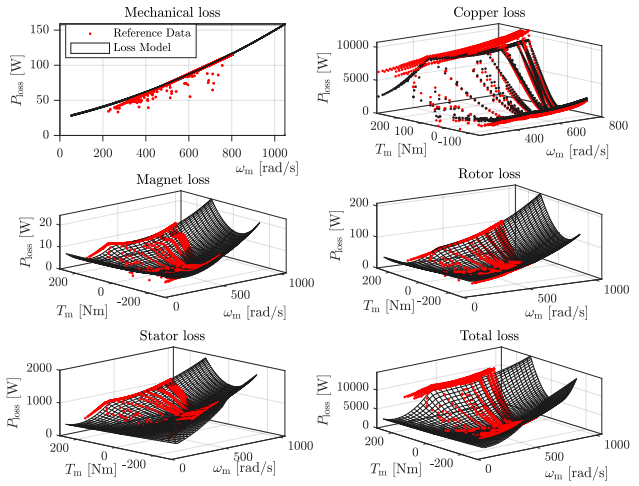

Fig. 4. The power loss models of the different components of the EM. Speed-dependent mechanical losses with $\mathrm{RMSE_{sf}} = 1.3\%$ (top left); speed-, power- and temperature-dependent copper losses representing the sum of the windings' and end-windings' losses with $\mathrm{RMSE_{wd}} = 5.9\%$ and $\mathrm{RMSE_{ew}} = 7.6\%$, respectively; speed- and power-dependent magnet losses with $\mathrm{RMSE_{pm}} = 5.9\%$ (center left); speed- and power-dependent rotor losses $\mathrm{RMSE_{rt}} = 4.8\%$ (center right); speed- and power-dependent stator losses $\mathrm{RMSE_{st}} = 3.7\%$ (bottom left); and speed- and power-dependent total losses $\mathrm{RMSE_{st}} = 7.1\%$ (bottom right).

domain, yielding the following almost-convex constraints:

$$\begin{cases} c_{\mathrm{sf}} \cdot \frac{\mathrm{d}}{\mathrm{d}s}\vartheta_{\mathrm{sf}}(s) \cdot v(s) = P_{\mathrm{sf}}(s) + k_{\mathrm{sf,rt}}(\vartheta_{\mathrm{rt}}(s) - \vartheta_{\mathrm{sf}}(s)) \\ c_{\mathrm{rt}} \cdot \frac{\mathrm{d}}{\mathrm{d}s}\vartheta_{\mathrm{rt}}(s) \cdot v(s) = P_{\mathrm{rt}}(s) + k_{\mathrm{sf,rt}}(\vartheta_{\mathrm{sf}}(s) - \vartheta_{\mathrm{rt}}(s)) \\ \qquad\qquad + k_{\mathrm{sf,rt}}(\vartheta_{\mathrm{pm}}(s) - \vartheta_{\mathrm{rt}}(s)) \\ \qquad\qquad + k_{\mathrm{rt,st}}(\vartheta_{\mathrm{st}}(s) - \vartheta_{\mathrm{rt}}(s)) \\ c_{\mathrm{pm}} \cdot \frac{\mathrm{d}}{\mathrm{d}s}\vartheta_{\mathrm{pm}}(s) \cdot v(s) = P_{\mathrm{pm}}(s) + k_{\mathrm{rt,pm}}(\vartheta_{\mathrm{rt}}(s) - \vartheta_{\mathrm{pm}}(s)) \\ c_{\mathrm{st}} \cdot \frac{\mathrm{d}}{\mathrm{d}s}\vartheta_{\mathrm{st}}(s) \cdot v(s) = P_{\mathrm{st}}(s) + k_{\mathrm{rt,st}}(\vartheta_{\mathrm{rt}}(s) - \vartheta_{\mathrm{st}}(s)) \\ \qquad\qquad + k_{\mathrm{st,wd}}(\vartheta_{\mathrm{wd}}(s) - \vartheta_{\mathrm{st}}(s)) \\ \qquad\qquad + k_{\mathrm{st},\infty}(\vartheta_{\infty} - \vartheta_{\mathrm{st}}(s)) \\ c_{\mathrm{wd}} \cdot \frac{\mathrm{d}}{\mathrm{d}s}\vartheta_{\mathrm{wd}}(s) \cdot v(s) = P_{\mathrm{wd}}(s) + k_{\mathrm{st,wd}}(\vartheta_{\mathrm{st}}(s) - \vartheta_{\mathrm{wd}}(s)) \\ \qquad\qquad + k_{\mathrm{wd,ew}}(\vartheta_{\mathrm{ew}}(s) - \vartheta_{\mathrm{wd}}(s)) \\ c_{\mathrm{ew}} \cdot \frac{\mathrm{d}}{\mathrm{d}s}\vartheta_{\mathrm{ew}}(s) \cdot v(s) = P_{\mathrm{ew}}(s) + k_{\mathrm{wd,ew}}(\vartheta_{\mathrm{wd}}(s) - \vartheta_{\mathrm{ew}}(s)), \end{cases} \tag{17}$$

where $P_i(s)$ is the power loss given by (16). Again, this set of equations is convex whenever speed is a given parameter. Depending on the material's characteristics, we constrain the temperature of each node as

$$\vartheta_{\mathrm{i}}(s) \leq \vartheta_{\mathrm{i,max}}, \tag{18}$$

in order not to damage the EM. The thermal limits $\vartheta_{\mathrm{i,max}}$ are shown in Table I.

TABLE I

THERMAL LIMITS OF THE NODES OF THE THERMAL NETWORK

Component	Max ϑ_{i} °C	Component	Max ϑ_{i} °C
Permanent Magnet	120	Shaft	170
Winding	200	Rotor	170
End winding	200	Stator	170

Finally, we consider two thermal scenarios: a cold-start lap, in which the motor temperature starts at the temperature of the coolant ϑ_{∞}, and a lap representing a long-run operation at steady-state. Mathematically, we characterize the scenarios as

$$\begin{cases} \vartheta_{\mathrm{i}}(0) = \vartheta_{\infty} & \text{if cold start} \\ \vartheta_{\mathrm{i}}(0) = \vartheta_{\mathrm{i}}(S) & \text{if long run.} \end{cases} \tag{19}$$

E. Battery Pack

In this section, we derive an energy-independent and a more accurate energy-dependent model of the battery dynamics. Even though the characterization and identification of these models were not specifically part of my master thesis project, they are presented for completeness as they are part of our publication [16].

The power at the terminals is $P_{\mathrm{b}}(s) = P_{\mathrm{dc}}(s) + P_{\mathrm{aux}}$, where P_{aux} is a constant auxiliary power. Converting this constraint to forces yields

$$F_{\mathrm{b}}(s) = F_{\mathrm{dc}}(s) + P_{\mathrm{aux}} \cdot \frac{\mathrm{d}t}{\mathrm{d}s}(s). \tag{20}$$

The internal battery power $P_{\mathrm{i}}(s)$, which causes the actual change in the battery state of energy $E_{\mathrm{b}}(s)$, is first approximated by $P_{\mathrm{i}}(s) = \alpha_{\mathrm{b}} \cdot P_{\mathrm{b}}(s)^2 + P_{\mathrm{b}}(s)$, where the efficiency parameter α_{b} is determined by a quadratic regression of the measurement data with a normalized RMSE of 0.96% [14]. This constraint can be translated into forces and relaxed as

$$(F_{\mathrm{i}}(s) - F_{\mathrm{b}}(s)) \cdot \frac{\mathrm{d}t}{\mathrm{d}s}(s) \geq F_{\mathrm{i}}(s)^2, \tag{21}$$

which can be expressed as a second-order conic constraint [4].

We include state-of-energy-dependency in the model of the battery by modeling the internal power to the terminal power through the open-circuit voltage U_{oc} and the internal resistance R as

$$P_{\mathrm{i}}(s) = P_{\mathrm{b}}(s) + \frac{R}{U_{\mathrm{oc}}^2} \cdot P_{\mathrm{i}}(s)^2,$$

which can be rewritten with the open-circuit power $P_{\mathrm{oc}} = \frac{U_{\mathrm{oc}}^2}{R}$ as

$$(P_{\mathrm{i}}(s) - P_{\mathrm{b}}(s)) \cdot P_{\mathrm{oc}}(s) = P_{\mathrm{i}}(s)^2. \tag{22}$$

Using a similar reasoning as in [19], the open-circuit power can be expressed by the piecewise affine approximation

$$P_{\mathrm{oc}}(E_{\mathrm{b}}) = a_{\mathrm{b}}^k \cdot E_{\mathrm{b}} + b_{\mathrm{b}}^k \cdot E_{\mathrm{b,max}} \quad \text{if} \quad E_{\mathrm{b}} \in [E_{\mathrm{b}}^{k-1}, E_{\mathrm{b}}^k] \quad \forall k \in [1, ..., K],$$

where $a_{\mathrm{b}}^k \geq a_{\mathrm{b}}^{k+1} \forall k \in [1, ..., K-1]$ and $b_{\mathrm{b}}^k \leq b_{\mathrm{b}}^{k+1} \forall k \in [1, ..., K-1]$ are parameters subject to identification, and K is the number of affine functions in the approximation. The proposed open-circuit power model is fitted in Fig. 5 with three affine functions. To secure convexity, we relax the open-circuit power to

$$P_{\mathrm{oc}}(E_{\mathrm{b}}) \leq a_{\mathrm{b}}^k \cdot E_{\mathrm{b}} + b_{\mathrm{b}}^k \cdot E_{\mathrm{b,max}} \quad \forall k \in [1, ..., K], \tag{23}$$

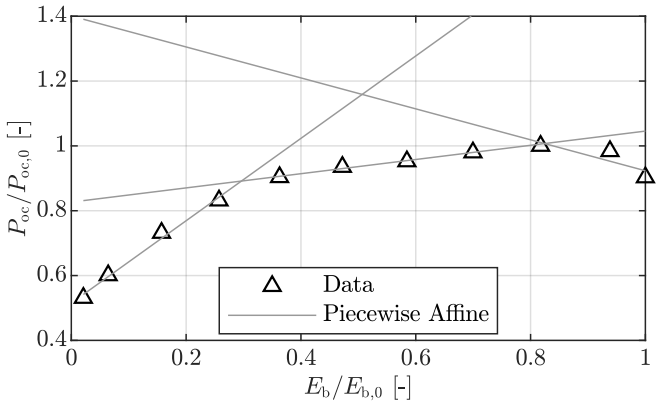

Fig. 5. A piecewise affine approximation of the battery open-circuit power P_{oc} as a function of the battery state-of-energy E_{b}.

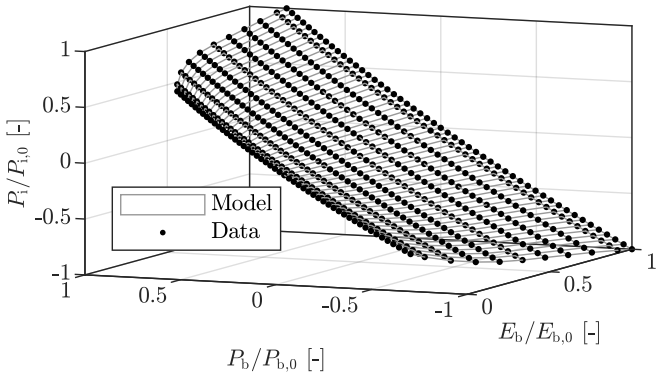

Fig. 6. The battery efficiency model using a piecewise affine approximation of the open-circuit power. The normalized RMSE is 0.08%.

Finally, relaxing (22) and converting it to forces yields

$$(F_{\mathrm{i}}(s) - F_{\mathrm{b}}(s)) \cdot \frac{P_{\mathrm{oc}}(s)}{v(s)} \geq F_{\mathrm{i}}(s)^2,$$

which can be written as the second order conic constraint

$$F_{\mathrm{i}}(s) - F_{\mathrm{b}}(s) + \frac{P_{\mathrm{oc}}(s)}{v(s)} \geq \left\| \begin{matrix} 2 \cdot F_{\mathrm{i}}(s) \\ F_{\mathrm{i}}(s) - F_{\mathrm{b}}(s) - \frac{P_{\mathrm{oc}}(s)}{v(s)} \end{matrix} \right\|_2. \quad (24)$$

The resulting energy-dependent battery model is shown in Fig. 6 and can approximate the nonlinear model with a normalized RMSE of 0.08%. The constraint (24) above is not fully convex, considering the quotient in the optimization variables $P_{\mathrm{oc}}(s)$ and $v(s)$. Yet again, we can recover convexity if speed is a given parameter.

The change in battery energy $E_{\mathrm{b}}(s)$ during the lap is defined as

$$\frac{\mathrm{d}}{\mathrm{d}s} E_{\mathrm{b}}(s) = -F_{\mathrm{i}}(s), \quad (25)$$

and is bounded as

$$E_{\mathrm{b}}(0) = E_{\mathrm{b},0}, \quad E_{\mathrm{b}}(S) = 0, \quad (26)$$

with $E_{\mathrm{b},0}$ as the energy available at the beginning of the lap.

Algorithm 1 Iterative Solving Procedure

$\bar{v}(s) \leftarrow$ Solve Problem 2
while norm$(v - \bar{v}) \geq \varepsilon_v$ **do**
  $\bar{v}(s) = v(s)$
  $v(s) \leftarrow$ Solve Problem 3

F. Minimum-lap-time Optimization Problem

In this section, we present an iterative algorithm used to solve the quasi-convex time-optimal control problem. The state variables for both the FGT and the CVT race car are $x = (E_{\mathrm{kin}}, E_{\mathrm{b}}, \vartheta_{\mathrm{sf}}, \vartheta_{\mathrm{rt}}, \vartheta_{\mathrm{pm}}, \vartheta_{\mathrm{st}}, \vartheta_{\mathrm{wd}}, \vartheta_{\mathrm{ew}})$. The control variables are $u = (F_{\mathrm{m}}, \gamma)$, where $\gamma(s)$ is present for the CVT only. The design variables for the FGT and CVT are $p_{\mathrm{FGT}} = \gamma_1$ and $p_{\mathrm{CVT}} = \gamma_{\max}$, respectively. We state the time-optimal control problem as follows:

Problem 1 (Full Nonlinear Problem)**.** *The minimum-lap-time control strategies are the solution of*

$$\min \int_0^S \frac{\mathrm{d}t}{\mathrm{d}s}(s)\,\mathrm{d}s$$
$$\textit{s.t. } (2) - (21), (23) - (26).$$

Due to the speed-dependency of the EM model, the battery model, and the thermal network, Problem 1 above is non-convex. In order to circumvent these non-convexities, we leverage the iterative Algorithm 1 based on the two following problems:

Problem 2 (Simplified Convex Problem)**.** *The minimum-lap-time control strategies for the thermally-unconstrained and speed-independent EM model and energy-independent battery model are the solution of the following second-order conic program (SOCP):*

$$\min \int_0^S \frac{\mathrm{d}t}{\mathrm{d}s}(s)\,\mathrm{d}s$$
$$\textit{s.t. } (2) - (8), (10) - (15), (20), (21), (25), (26).$$

Problem 3 (Thermal Speed-dependent Convex Problem)**.** *Given a velocity profile $\bar{v}(s)$, the minimum-lap-time control strategies are the solution of the following SOCP:*

$$\min \int_0^S \frac{\mathrm{d}t}{\mathrm{d}s}(s)\,\mathrm{d}s$$
$$\textit{s.t. } (2) - (8), (10) - (14), (16), (18) - (20), (23) - (26),$$
$$\textit{and } (9),\ (17),\ (24) \textit{ with } v(s) = \bar{v}(s).$$

Algorithm 1 leverages the speed profile of the solution of the speed-independent Problem 2 as an initial guess for $\bar{v}(s)$ to solve the speed-dependent Problem 3, iterating on it until two consecutive speed profiles coincide up to a certain tolerance $\varepsilon_v > 0$.

G. Optimality Considerations

In this section, we reason on the convergence and optimality properties of Algorithm 1 and we introduce how we can leverage standard non-linear programming to solve Problem 1. A detailed initial mathematical analysis showing injectivity properties for the mapping between $\bar{v}$ and v_{CVX}

can be found in Appendix H. Such a property excludes the possibility of an abrupt and exact convergence in a finite numbers of iterations.

To prove convergence and optimality of Algorithm 1 as a solution to Problem 1, one possibility is to show that the iteration of Algorithm 1 is contractive and hence it has a unique fixed point (Banach fixed-point theorem), and to show that the fixed point—namely a KKT point (and global optimum) of Problem 3 with $\bar{v} = v_{\mathrm{CVX}}$—corresponds to a KKT point of Problem 1, possibly the global optimum. Such a proof requires a careful study of both problems, and we leave it for future research. Nonetheless, the numerical results presented in Section III-F suggest that, while Algorithm 1 seems to be indeed contractive, it does not seem to precisely converge to the KKT point (local optimum) found by solving Problem 1 with standard nonlinear programming methods, albeit providing a comparably time-optimal solution.

We proceed by partially evaluating the KKT conditions of Problem 1 and Algorithm 1 to explore other properties. We know that Algorithm 1 and Problem 1 have very symilar formulations which are reflected in their KKT conditions. The two Lagrangians are equivalent in all the constraints which do not include $\bar{v}$, hence we focused only on the constraints which result in different terms. We identify three sets of constraints in which $\bar{v}$ is present: transmission (9), power loss models (16) and thermal network nodes (17). In the convex iterations, these constraints are all speed-independent because they only include $\bar{v}$ which is constant per iteration. Therefore, they do not contribute to the derivative of the Lagrangian with respect to speed. However, the constraints are speed-dependent in the nonlinear case resulting in non zero terms in the Lagrangian derivative. This suggests that since both sets of KKT conditions have to be satisfied by the same solution, the non-zero terms of the nonlinear Lagrangian speed derivative should amount to zero. This was not verified, therefore $x^{\star}_{\mathrm{CVX}}$ is not necessarily a KKT point for Problem 1. We leave a more detailed analytical study of the KKT conditions to further research.

We use standard nonlinear programming to solve Problem 1. We use such a solution for comparison and the nonlinear structure to run other practical tests to discuss the KKT conditions. The NLP solver solves the KKT conditions of the problem. We can start by checking the feasibility conditions of the NL constraints, because if the solution of Algorithm 1 is not feasible, it is not a KKT point. It is important to note that the nonlinear solver evaluates the KKT conditions with a certain tolerance. Therefore, a particular set of solutions may not seem a KKT point due to numerical errors. We can also directly test the solution of Algorithm 1 on the KKT conditions of Problem 1 by using the solution of Algorithm 1 as the initial guess for Problem 1. If the solver moves from the initial guess, it implies that the initial guess does not solve the KKT conditions of Problem 1 at the first iterations. The results of these tests are presented in Section III-F.

H. Discussion

A few comments are in order. First, we model both the FGT and the CVT with a constant efficiency—a common approach for high-level modeling purposes—since the focus of this paper is not on the transmission modeling itself, and we refer readers interested in this topic to [5]. Second, we identify the EM power loss and thermal model by pre-studying the system and gaining knowledge of likely operational areas. Therefore, the accuracy of the results might be worse for a different race track. This is due to the convex approximations of the nonlinear power losses and the error propagation on the temperatures. The rise in temperature of each of the nodes is proportional to the heat generated in the node and the heat transferred to the neighboring nodes. Therefore, an error in the node's power loss influences the temperature's slope of the node. If the motor operates in areas where the power loss error has always the same sign (either under- or over-estimation), the temperature of the node diverges from the temperature evaluated by the high fidelity software. Third, the thermal network operates using the average temperatures and they are constrained in the time-optimal control problem. We use the average temperatures to maintain the physical meaning of the thermal network, but the optimization should constrain the maximum temperatures. The relation between average and maximum temperatures of windings, end-windings and permanent magnets will be investigated in future research. Fourth, we assume the battery to be able to accommodate any EM power request. This assumption is acceptable for high-performance batteries designed for fast-charging applications. Fifth, we begin the study of optimality for Algorithm 1 with promising results. We uncovered multiple properties which can be used for future research to conclusively state the accuracy of the method. Finally, nonlinear solvers are known to be highly dependent on the warm-start position. In the chapter below, we will present the convenience of the NL solver. The solver performs well only because it was given a good set of initial conditions. However it does not converge if all the scaled variables are initialized to one.

III. Numerical Results

This section studies the performance achievable by an electric race car equipped with two identically operated EMs connected to an FGT and a CVT in different operating scenarios on the Le Mans race track. We first discuss the results obtained for an FGT-equipped car in a cold-start scenario and compare it with the thermally-unconstrained solution. Thereby, we also validate our results with the high-fidelity EM software Motor-CAD and a nonlinear battery model. Moreover, we study the time-optimal strategies under a long-run steady-state operation, comparing the FGT- and CVT-equipped vehicles. Similarly, we analyse the time-optimal strategies for a scarce battery energy case to identify differences and similarities. Furthermore, we compare the solutions of Algorithm 1 and Problem 1. Finally, we discuss the optimality of Algorithm 1, with practical and theoretical considerations.

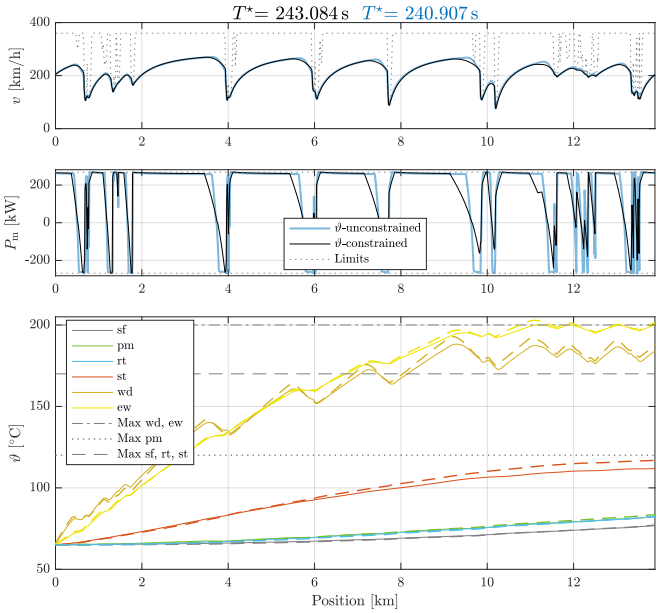

Fig. 7. The speed, the motor power and the EM components' temperature of an FGT-equipped vehicle in a cold-start scenario. The bottom graph additionally shows the overheating temperature limits and a validation by comparing it with a Motor-CAD simulation. The results are presented by the solid lines and the Motor-CAD validation data is presented by the dashed lines.

We set the weight of the FGT- and CVT-equipped vehicles to 1342 kg and 1393 kg, respectively. Furthermore, we set the EM-to-wheels efficiency of the FGT-equipped car to 98 %, whilst assuming a lower average value of 96 % for the CVT-equipped car [5], [14].

We discretize the model presented in Section II with a step-size of 10 m using the trapezoidal method in order to avoid numerical instabilities stemming from the LPTN. An analytical and numerical comparison with the classical Euler forward integration scheme is presented in Appendix D. We compute the solution using two methods. First, we parse the problem using YALMIP [20] and solve it with the second-order conic solver ECOS [21]. Second, we parse and solve the nonlinear problem using the nonlinear solver IPOPT [22] in a CasADi [23] implementation. One iteration of Algorithm 1 takes about 53 s to parse and 34 s to solve when using a 2.3 GHz Quad-Core Intel Core i5 processor with 8 GB of RAM. The solution converges typically within four to six iterations, resulting in an average total computation time of 7-8 min, including overhead.

A. FGT Cold Start

Using Algorithm 1, we first optimize the FGT-equipped powertrain for a cold-start scenario and we compare the thermally-constrained and unconstrained solutions. Fig. 7 shows the results, whereby the lap time of the thermally-constrained solution is 2.1 s slower than the lap time of the thermally-unconstrained solution. From the motor power trajectory, we observe that the thermal constraints do not hinder the motor from operating at maximum power. However, the optimal gear ratio γ_1 decreases from 4.54 for the thermally-unconstrained problem to 3.83 for the thermally-constrained problem. This is a direct result of the EM losses generation. As can be seen from Fig. 4 the speed attributes more than torque at the heating of the EM. Therefore, a smaller gear ratio invites the motor to operate at higher torques and lower speeds.

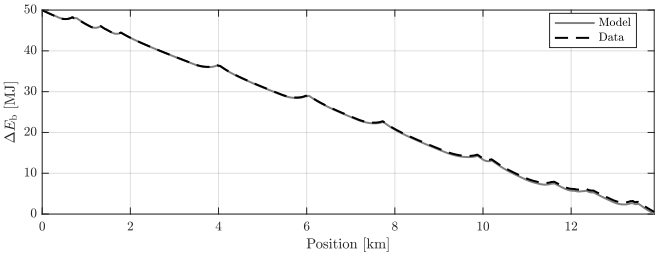

Fig. 8. The validation of the battery energy consumption obtained by the solution, represented in continuous lines, and in dashed lines the resulting battery energy consumption using Motor-CAD loss model and a nonlinear battery model. The relative drift in energy at the end of lap is equal to 1.1%.

It can also be observed that the EM is using regenerative braking in both cases, although the thermally-constrained operation shows a more gradual approach to the negative power region. The thermal constraints attempt to limit the absolute value of the output power because of its dependency with the power losses. As a result, the low-power operations of the EM are extended to reduce the temperature rise or to briefly cool down the EM components.

The lower subfigure of Fig. 7 shows the temperature evolution of the motor components. As can be seen, the end-windings are the component limiting the operation of the motor by reaching the thermal limit towards the end of the lap. Fig. 7 also indicates the temperature trajectory of the EM simulated in Motor-CAD while subjected to the EM duty cycle of the thermally-constrained solution. We can observe that our models can closely reproduce the results stemming from a high-fidelity simulator, resulting into a cumulative drift below 2 °C for all the EM components except the stator, which achieves an error of 5 °C while staying well below its limit of 170 °C.

We validate the power loss model and the battery model in Fig. 8, showing the state-of-energy trajectory of our model compared to the one resulting from Motor-CAD and a nonlinear battery model. As can be seen, the small deviation between the two solutions results in a total drift of 1.1 %.

B. FGT Long Run

The trends observed in the cold-start scenario are much more clearly emphasized in a long-run operation where the EM is at a higher temperature. Fig. 9 shows the performance and the temperature trajectory obtained with Algorithm 1, of the FGT-equipped car during the lap, whereby the lap time is more than 10 s longer than in the unconstrained case, highlighting the prominent impact of the thermal constraints on the time-optimal strategies. Hereby, the more gradual transition into regenerative braking is emphasized to the extent that energy regeneration is almost never allowed in order to reduce the EM losses and, in turn, the components'

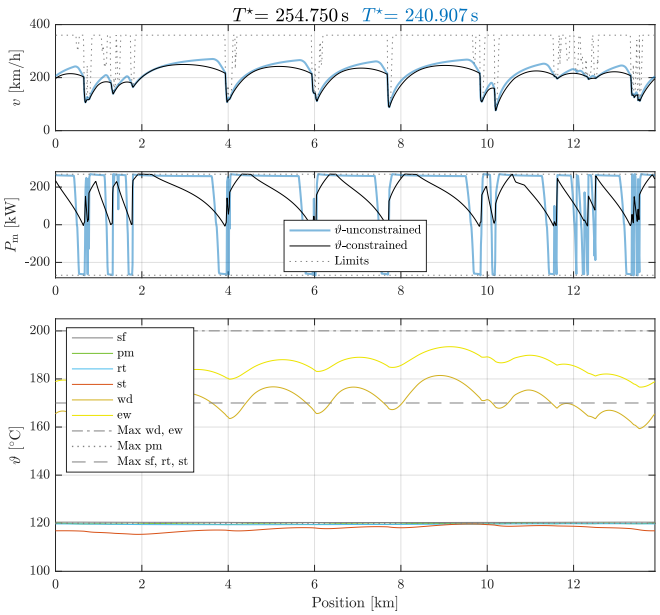

Fig. 9. The speed, the motor power, and the EM components' temperature of an FGT-equipped race car during a long-run operation.

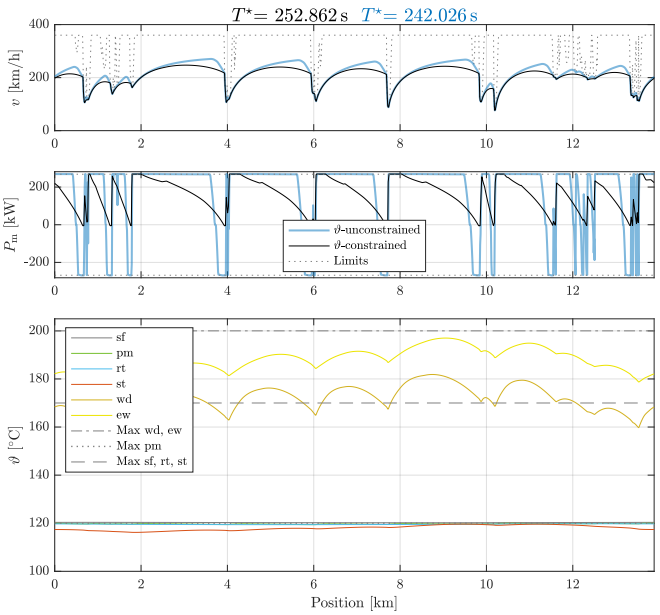

Fig. 10. The speed, the motor power and the EM components' temperature for a CVT-equipped race car during a long-run operation.

overheating. Interestingly, and in contrast to the cold-start scenario, in this case the EM power is limited by the temperature of the permanent magnets, mildly oscillating in the vicinity of their thermal boundary.

C. CVT Long Run

Finally, we showcase our models for a CVT-equipped race car to study the impact of different transmission technologies on achievable performance during a long-run operation, solving Algorithm 1. Fig. 10 shows the numerical results of this scenario, where it is possible to observe a similar response as in the FGT-equipped car. Similar to the FGT, the optimal maximum CVT gear ratio γ_max is reduced from 6.5 in the thermally-unconstrained case to 5.5 for the thermally-constrained lap. Moreover, when coupled with a CVT, the EM shows intense regenerative braking in the thermally-unconstrained case, and almost no regeneration when the temperature constraints are active, whilst, also in this case, the permanent magnets are the limiting factor.

With respect to lap times, the thermally-unconstrained solution shows that the EM coupled with an FGT would be 1.12 s faster than when coupled with a CVT, since the CVT cannot compensate its higher weight and lower efficiency with its ability to control the EM in a more efficient fashion. However, under a thermally-constrained long-run scenario, a more efficient EM operation not only improves the energy consumption, but also reduces overheating, so that the CVT-equipped car can significantly outperform the FGT-equipped car with a 1.89 s faster lap time.
For completion, the "CVT Cold Start" results are presented in Appendix E.

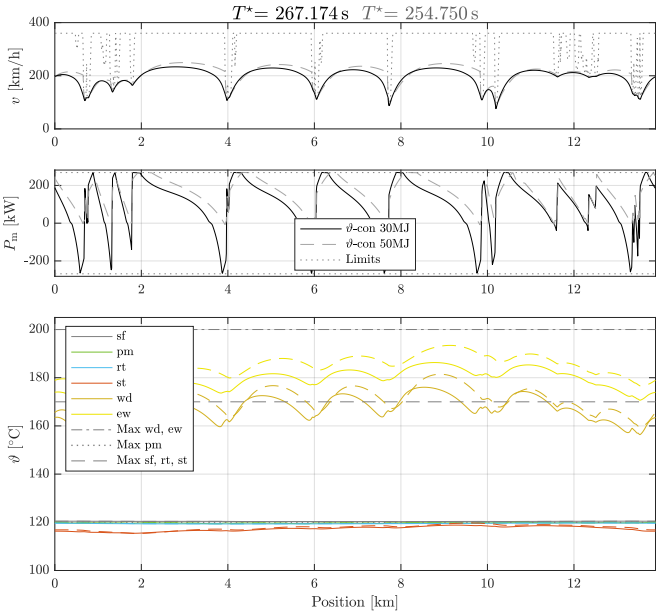

Fig. 11. The speed, the motor power and the EM components' temperature for a FGT-equipped race car during a long-run operation, considering a scarce and an abundant battery energy scenarios. The bottom graph represents the temperatures in the two cases: scarce as a straight line and abundant as a dushed line.

D. Scarce Battery Energy, FGT Long Run

As mentioned in the previous sections, the battery energy can be a limiting factor. Fig. 9 shows that for the given battery energy, the vehicle should not recuperate the energy during breaking. It is clear that this behavior is admissible only if there is an abundance of battery energy. Therefore, we study the effect of scarce battery energy scenarios by reducing the battery energy for one lap from 50 MJ to 30 MJ. The numerical results are presented in Fig. 11. As can be

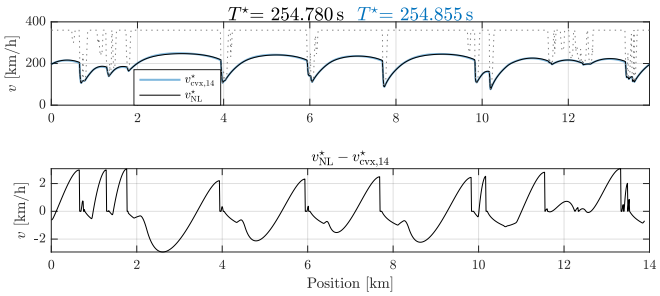

Fig. 12. The speed of the nonlinear solution and Algorithm 1 and difference between the two solutions for a FGT-equipped race car during a long-run operation.

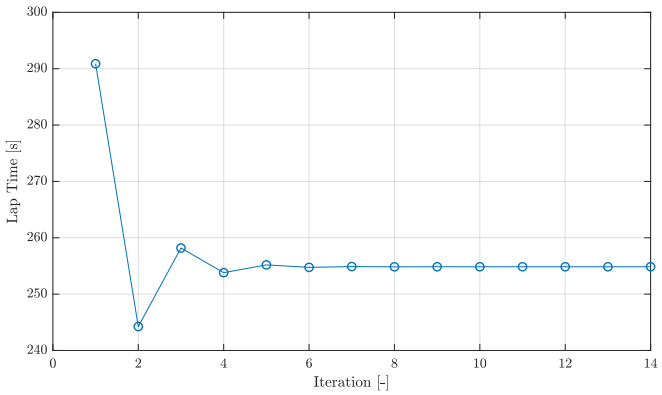

Fig. 13. Lap time value per iteration with a speed norm error of 1e-6. The lap time of the last iteration is 254.855 s.

seen, the lap time is considerably reduced. The time-optimal control strategy is more energy-conservative and it includes deep energy regeneration during braking. Moreover, the temperature trajectories of the two cases reflect the energy dependent strategy. A lower output power implies less power loss and lower temperature but also lower speed and more time to extract heat from the EM. However, deep regenerative operations cause higher power losses. To conclude, it can be observed that the energy conservative strategy suggests a slower pace during straightaways to allow the EM to cool down. This prepares the EM for the turns where the vehicle recuperates energy in breaking and exits the turns more aggressively than the energy-abundant scenario.

E. Comparison with NLP Solver

We parse the nonlinear Problem 1 using CasADi [23] and solve it for the FGT-equipped powertrain during a long-run operation, using the nonlinear solver IPOPT [22] CasADi takes about 0.53 s to parse and IPOPT solves it in 45 s. However, these numbers strongly depend on the initial conditions. In fact, Problem 1 could not be solved without a warm start, highlighting the importance of leveraging convex optimization methods in the solution process. In this case, the initial conditions are assumed as the solution of the simplified convex Problem 2 and as constants for the variables that are not present in Problem 2.

The complete numerical solutions are presented in Appendix F. It can be observed that the solutions are very close. The temperature behavior is almost unvaried with a permanent magnet limited operation. There are minor differences in the speed profile which can be seen in Fig. 12. The speed generally match during the turns, reaching the physical limitation of the system. After isolated turns between straights, the nonlinear solution uses a more conservative approach by accelerating less in the straight. However, it reaches higher maximum speeds and it suggests a more aggressive strategy when approaching a turn.

The iterative nature of Algorithm 1 is reflected in an oscillating lap time converging to 254.855 s as shown in Fig. 13. The nonlinear optimal solution is almost a tenth of a second faster than Algorithm 1's solution. Even though this difference could be substantial in the real application, we are comparing methods, not solutions. With this in mind, the difference in lap time is small and could be due to numerical error. The constraints formulations of the nonlinear and convex problem are different. The former uses geometric means, while the latter implements second order conic constraints. This could lead to numerical diffrences. Therefore, we re-write Algorithm 1 using CasADi and we solve it with IPOPT. The method converges to a lap time of 254.838 s which differs from both the solutions presented in Fig. 12. This implies that there are numerical errors but they are not the only factors. We can see that also from the speed discrepancy. While the lap times difference is about 0.04% which could be attributed to numerical errors, the speeds' difference is around 1%. This shows a concrete difference between the two solutions, related to the methodologies. In the following section, we present some numerical evaluations to identify such differences. For completion, we present the "FGT Cold Start" and the "CVT long run" results in Appendix G.

F. Optimality Considerations, Results

Whilst we know that the nonlinear solver has converged to a local minimum, we need to discuss the optimality of Algorithm 1. This Section presents the numerical verifications mentioned in Section II-G.

We mentioned how to leverage the contractive property of Algorithm 1 by discussing the optimality of the solution. Fig. 14 shows that the solution of the iterative method becomes closer to a fixed point at each iteration. This suggests to be contractive, hence to possess a unique fixed point. However, Fig. 15 suggests that Algorithm 1 converges to a solution which is not the optimal solution found by the NLP. Therefore, it seems that its unique fixed point may not correspond to a KKT point of Problem 1.

There are other practical ways to verify if the solution of Algorithm 1 is a KKT point of Problem 1. For these evaluations, we use the most precise convex solution we have, $x^\star_{\mathrm{CVX},14}$. The first is to check the feasibility conditions of Problem 1 with $x^\star_{\mathrm{CVX,i}}$. We know that $x^\star_{\mathrm{NL}}$ is a solution of Problem 1 for a particular tolerance and we desire to check if the $x^\star_{\mathrm{CVX},14}$ can solve the feasibility conditions with similar tolerance. Fig. 16 shows the permanent magnets

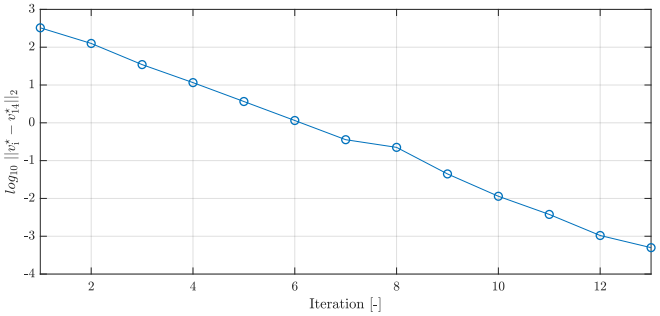

Fig. 14. Algorithm 1 contractive property verification using $v_{14}^\star$ as a fixed point.

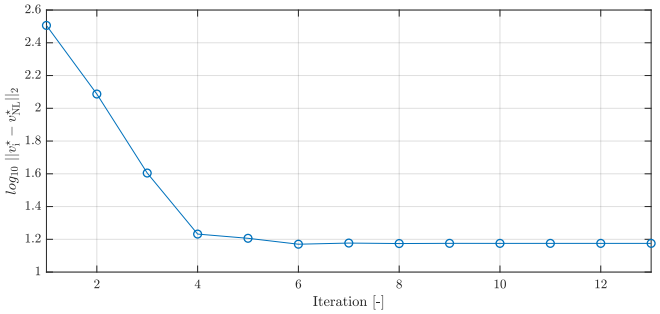

Fig. 15. Algorithm 1 contractive property verification using $v_{NL}^\star$ as a fixed point.

nonlinear active constraint in FGT long run case: logarithmic of Eq. 17 with all the terms on the same side equalling zero. It becomes evident that the nonlinear problem satisfies such a constraint with an almost 3 orders of magnitude higher accuracy. Similar results could be seen by comparing the permanent magnet material thermal limit constraint. The nonlinear problem is again 2 orders of magnitude more accurate. However, these absolute error values are very small, i.e., 2.5e-7 . We can conclude that $x^\star_{\mathrm{CVX},14}$ satisfies the feasibility conditions of the limiting constraints with what we can consider a neglectable tolerance.

Solving Problem 1 using $x^\star_{\mathrm{CVX},14}$ as starting point yields the same $x^\star_{\mathrm{NL}}$ described in the previous section. This could happen because of the feasibility tolerance or because $x^\star_{\mathrm{CVX},14}$ is not a KKT point for Problem 1.

We started the discussion of Algorithm 1's properties proving its injective structure and partially solving and comparing the KKT conditions. In order to study Algorithm 1 we researched the literature for similar known methods. By considering $\bar{v}$ as a variable, we can characterise Algorithm 1 as an alternating coordinate method, subgroup of block coordinate methods. These methods are usually defined as Algorithm 2, [24]. The literature offers a large number of documentations regarding these methods, providing extensive discussions on convergence rates and optimality conditions. Algorithm 1 aims to satisfy the constraint $v = \bar{v}$ with a certain tolerance without optimizing $\bar{v}$, which makes it different to a standard alternating coordinate method. Therefore, we leave a more profound and formal analysis of these methods to future research.

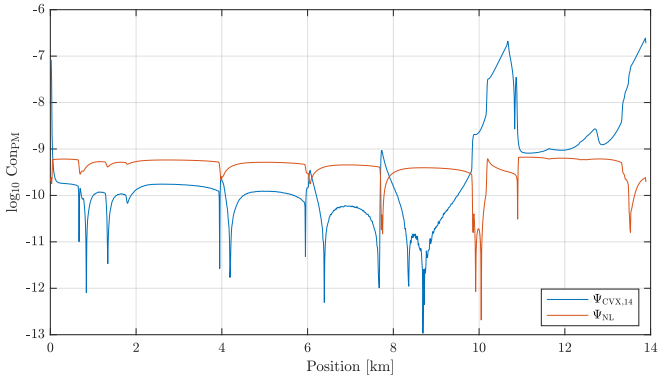

Fig. 16. Permanent magnets thermal network equality constraint in FGT-equipped race car during a long-run operation, solving Algorithm 1 and Problem 1.

Algorithm 2 General form of block coordinate method [24]

while [condition] **do**
  k=k+1;
  Pick $\mathrm{b_k} \in \{1, 2, ..., s\}$; deterministic or random
  fix blocks $\{\{1, 2, ..., s\} - \{\mathrm{b_k}\}\}$
  Solve

IV. Conclusion

In this paper, we studied the impact of thermal limits in electric car racing. To this end, we devised a quasi-convex and a nonlinear optimization framework, accurately capturing the temperature dynamics of an interior permanent magnet electric motor (EM) using a thermal network including the stator, the rotor, the permanent magnets, the windings and the end-windings. We validated our models with the high-fidelity EM simulation software Motor-CAD and a nonlinear battery model, showing a cumulative drift of about 1% for both the temperatures and the battery energy. When showcasing our framework on the Le Mans racetrack for a car equipped with a fixed-gear transmission and different operating scenarios, we concluded that the main components limiting the EM performance are the end-windings in a cold-start scenario and the permanent magnets during a long-run operation. We observed that thermal limitations can result in a significant lap time loss which can, however, be partially salvaged by equipping the race car with a continuously variable transmission. Furthermore, we showed how the availability of battery energy influences the regeneration operation. Finally, we began investigating the properties of the proposed iterative algorithm based on second-order conic programming with respect to standard nonlinear programming. Our iterative algorithm is much slower and it converges to a presumably locally optimal solution. However, the nonlinear problem time and success is highly dependent on the initial conditions. The nonlinear framework convergency rate is very fragile (i.e., the CVT cold-start scenario did not converge). All in all, we can combine the convergence of the iterative algorithm with the optimality of the nonlinear solver. If we concatenate the nonlinear solver to the last iteration such that it uses

the iterative solution as a starting point, we are very likely to converge to a provably locally optimal solution in a predictable time span.

This work opens the field for several extentions. First, our promising preliminary results prompt a more detailed analysis based on high-fidelity models. Second, we are interested in exploring the application of multi-speed gearbox transmissions, as they combine a low mass and high efficiency with the ability to operate at multiple transmission ratios. Third, we suggest modifying the proposed iterative algorithm to a general block-coordinate method form. This method allows to perform theoretical analyses to examine whether the almost-convex problem structure could be leveraged in order to guarantee optimality of the solutions. Fourth, we have seen how the battery energy availability influences the EM control strategy, and we would like to extend the investigation of this behavior in the context of a battery thermal model. Finally, we would like to leverage the proposed offline frameworks to devise temperature-aware minimum-lap-time control algorithms in the context of a full race. This scenario may include strategical decisions such as pitstops and takeovers which are isolated events that imply brief cooling and overheating.

ACKNOWLEDGMENT

I thank Dr. I. New for proofreading this thesis report. I desire to thank Mouleeswar Konda for his involvement in designing the thermal network and Olaf Borsboom for his contributions to the battery model and almost-convex optimization framework. I thank Professor Theo Hofman for the mentoring he provided during my studies and Professor Steven Wilkins and Professor Tijs Donkers for accepting to be part of my examination committee. Finally, I would like to thank Professor Mauro Salazar, the supervisor of this study, for his enthusiasm, dedication and patience which helped me not to lose motivation and grit in these difficult times.

APPENDIX

A. Indentification EM

Fig. 17 shows the identification of $T_{\max}$, $c_{\mathrm{m},1}$ and $c_{\mathrm{m},2}$ while Fig. 18 presents the identification of α_{m}.

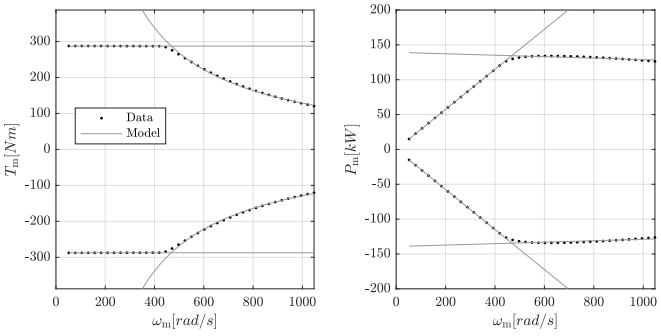

Fig. 17. Identification of $T_{\max}$, $c_{\mathrm{m},1}$ and $c_{\mathrm{m},2}$ from Motor-CAD data.

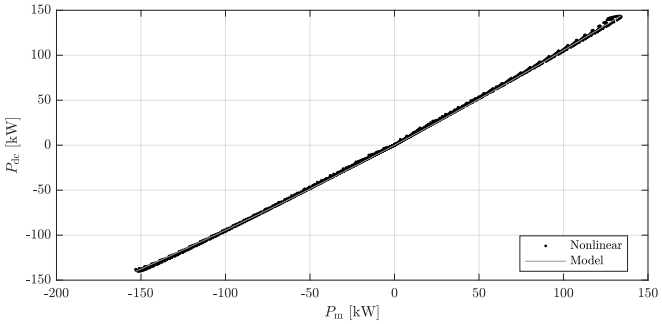

Fig. 18. Identification of α_{m} from Motor-CAD data.

B. EM Duty Cycle

We define a EM duty cycle to evaluate the electric motor power loss data which is used to identify our models. The duty cycle is inspired by the EM operations of the temperature-unconstrained problem, such that we minimize the fitting error in the regions where the motor is expected to operate, Fig. 19. We also consider a negative fraction of the EM operations to impose a good fit in the regeneration half plain.

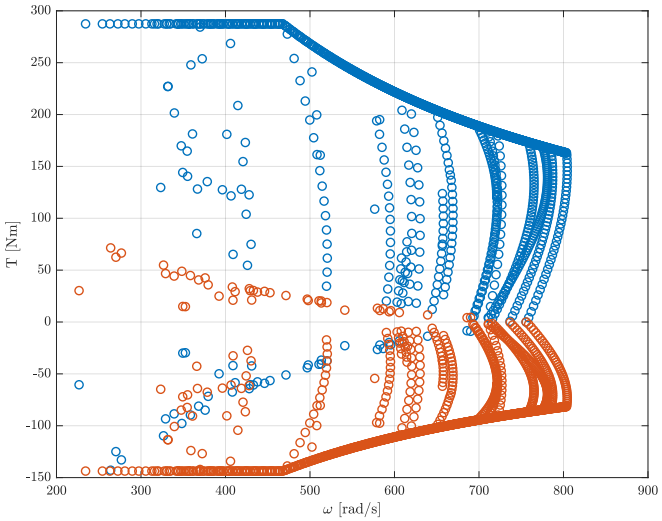

Fig. 19. EM Duty cycle used to fit the power loss model and the thermal network.

We choose this fraction to be 0.5 for multiple reasons. First, the EM operations derive from thermally unconstrained simulations. Since the simulation in Motor-CAD is a “cold start”, the temperatures gradually increase, allowing the fit over a wide range of temperatures. In any case, we expect at least one node to reach a temperature close to or higher than its thermal limit by the end of the cycle. If we add a second cycle to obtain a better fit we cannot use additional high power operation because they would generate temperatures outside our range of interest. Therefore, additional operations have to be such that the power loss is low enough for the temperature to decrease. Second, deep regeneration operations imply higher losses, as well as high power operations. The former is beneficial for energy-saving

reasons, while the latter reduces the lap time. Since lap time is the objective function, high power operations will be preferred for abundant battery energy. The importance of regenerative operations increases for scarce battery energy scenarios. Therefore, we expect the available energy to have a relevant impact on the EM control strategy. We investigate the difference in control strategy between abundant and scarce battery energy and we use the same regeneration power model. The value of the negative fraction influences where the model is more representative of reality. Therefore, we choose 0.5 as a compromise to obtain an averagely accurate regeneration model instead of sacrificing some areas in favor of others.

C. Power and Temperature Fit Result

Fig. 20 presents the comparison between the power loss data obtained with Motor-CAD and the estimated power loss using the convex quadratic model.

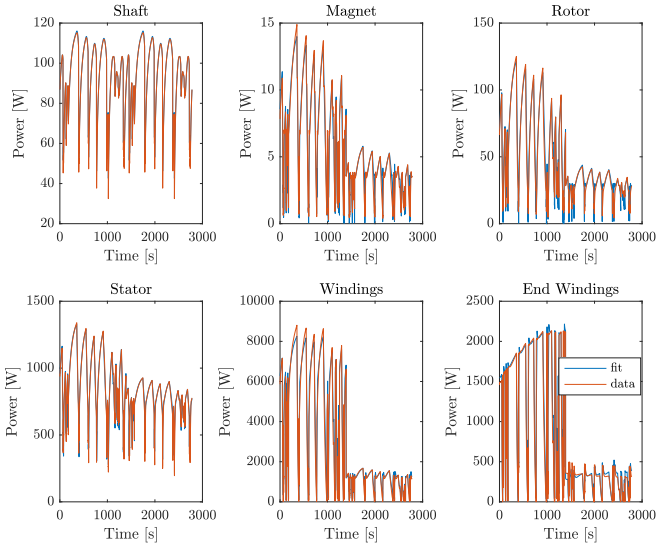

Fig. 20. Comparison between the power loss models with data obtained by Motor-CAD, for the different components of the EM. Speed-dependent mechanical losses with $\mathrm{RMSE}_{\mathrm{sf}} = 1.3\%$ (top left); speed-, power- and temperature-dependent copper losses representing the sum of the windings' and end-windings' losses with $\mathrm{RMSE}_{\mathrm{wd}} = 5.9\%$ and $\mathrm{RMSE}_{\mathrm{ew}} = 7.6\%$, respectively; speed- and power-dependent magnet losses with $\mathrm{RMSE}_{\mathrm{pm}} = 5.9\%$ (center left); speed- and power-dependent rotor losses $\mathrm{RMSE}_{\mathrm{rt}} = 4.8\%$ (center right); speed- and power-dependent stator losses $\mathrm{RMSE}_{\mathrm{st}} = 3.7\%$ (bottom left); and speed- and power-dependent total losses $\mathrm{RMSE}_{\mathrm{st}} = 7.1\%$ (bottom right).

Fig. 20 presents the comparison between the power loss data obtained with Motor-CAD and the estimated power loss using the convex quadratic model.

D. Trapezoidal Method

Fig. 22 presents the instability of the thermal network when using Euler forward integration. The figure is a sufficient proof of the presence of instabilities. The discreet time problem is written in state space model $\dot{x} = Ax$ where x contains the temperature of the nodes. We study the eigenvalues of matrix A in case of Euler forward or

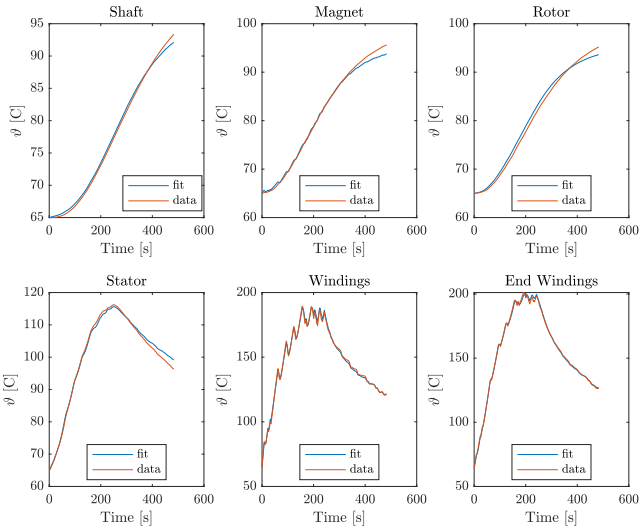

Fig. 21. Nodes temperature results of the thermal network parameter identification. The collective root mean square error is $0.82\,^{\circ}\mathrm{C}$.

trapezoidal integration. The sets of eigenvalues for $c_{\mathrm{pm}} = 9$ are

$$\lambda_{\mathrm{EulFor}} = \begin{bmatrix} -1.7373 \\ 0.9630 \\ 0.9882 \\ 0.9912 \\ 1.0001 \\ 0.9969 \end{bmatrix} \qquad \lambda_{\mathrm{Trap}} = \begin{bmatrix} -0.1556 \\ 0.9637 \\ 0.9883 \\ 0.9912 \\ 1.0001 \\ 0.9969 \end{bmatrix}$$

For discrete time operations the eigenvalues must be within the unit disk to ensure stability. As can be seen, the eigenvalues reveal that the instability is related to the integration method. Therefore, we use trapezoidal integration.

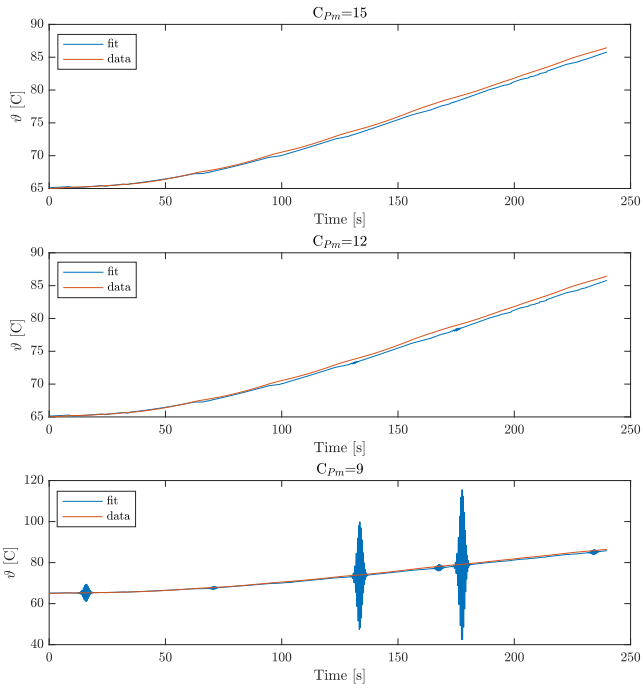

Fig. 22. Instability of the thermal network when using Euler forward integration for different values of c_{pm}.

E. CVT Cold Start

Fig. 23 shows the numerical results of the CVT cold start scenario. The results are consistent with the discussions presented for the previous cases. It is possible to observe that the temperature divergence is bigger than FGT cold start. The reason is related to the convex approximation of the losses and it is presented in the EM section while introducing the power loss model and the duty cycle fit Fig. 19. We approximate the nonlinear power loss with a convex approximation. The errors in the power loss estimation influences the slope of the temperature through the thermal network Eq. 17. In other words, the persistency of a particular sign in the error results in an increasing divergence between estimated and real temperatures. In order to avoid this phenomenon, we have built a duty cycle of likely operational points. To achieve better thermal representation it is suggested to incorporate some characteristic of the CVT-equipped EM behavior in the duty cycle used to identify the power loss and thermal network models.

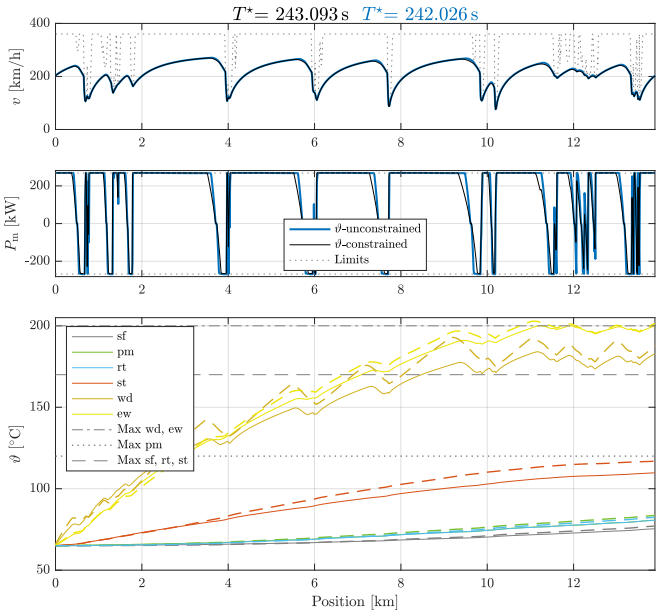

Fig. 23. The speed, the motor power and the EM components' temperature of a CVT-equipped vehicle in a cold start scenario. The bottom graph additionally shows the overheating temperature limits and a validation by comparing it with a Motor-CAD simulation. The results are presented by the solid lines and the Motor-CAD validation data is presented by the dashed lines.

F. NLP SR Long Run

Fig. 24 shows the numerical results on the same format as the other cases. As can be seen, the results are almost identical.

G. NLP Other Simulations

For completion, we present the results of CVT-equipped long run Fig. 25 and FGT-equipped cold start Fig. 25. The latter presents also the validation data. It can be noted that the nonlinear (solid lines) and almost convex solutions (thin dashed lines) are almost identical.

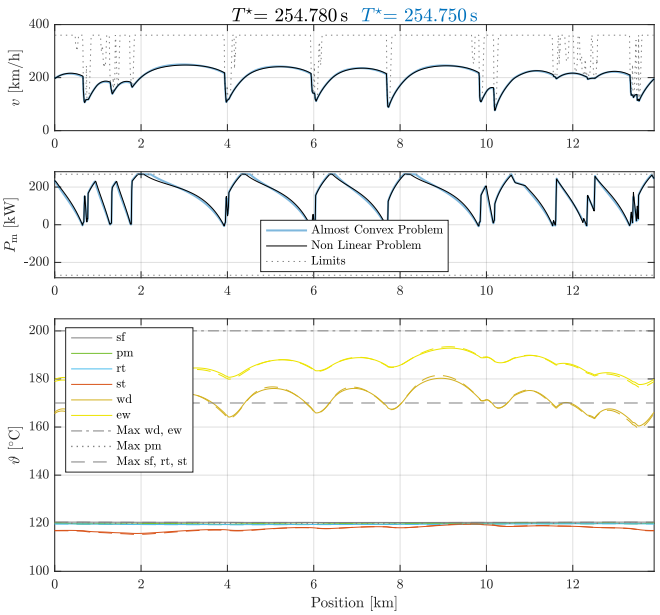

Fig. 24. The speed, the motor power and the EM components' temperature for a FGT-equipped race car during a long-run operation, computed by nonlinear IPOPT and Algorithm 1

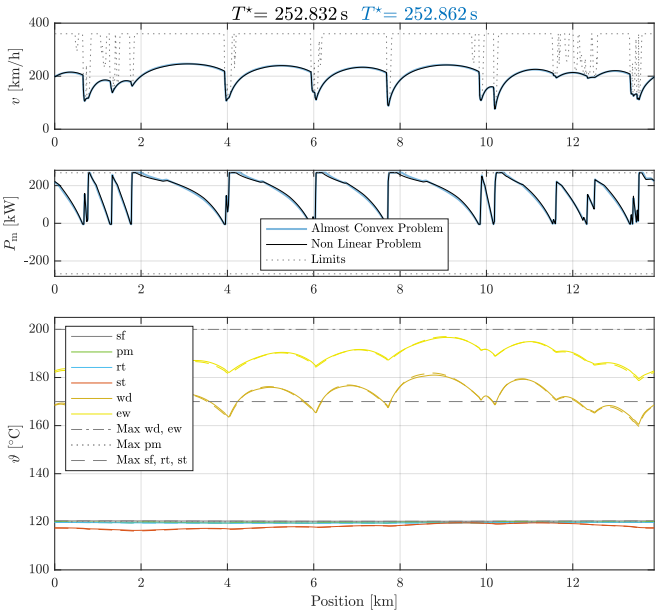

Fig. 25. The speed, the motor power and the EM components' temperature for a FGT-equipped race car during a long-run operation, computed by nonlinear solver IPopt and Algorithm 1.

H. Initial Analysis of Algorithm 1

In this section we discuss the optimality of Algorithm 1. First, we prove that the convex Problem 3 has a injective structure in speed. Second, we discuss what type of convergence we could expect from Algorithm 1. Finally, we discuss further analyses to study convergence. As mentioned previously, we analyse the convex transformation of Problem 3 from the design space and a constant speed $\bar{v}$ to the optimal solution $x^\star_{\mathrm{CVX}}$, Algorithm 1 which is

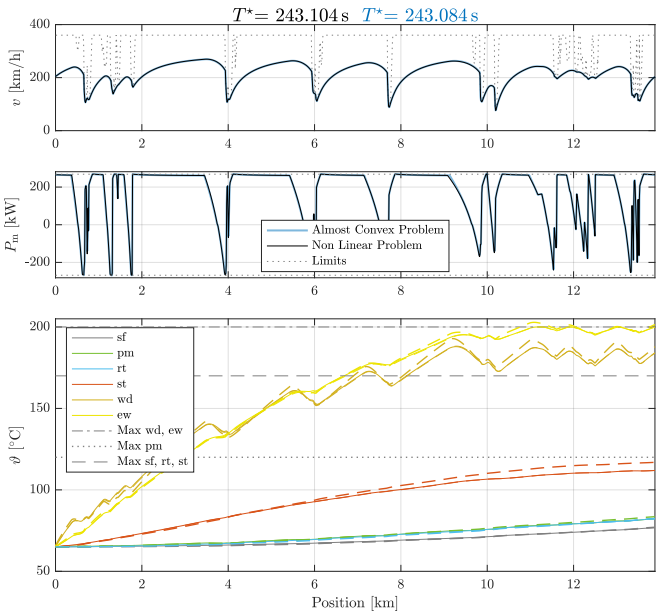

Fig. 26. nonlinear optimal solution. The speed, the motor power and the EM components' temperature of an FGT-equipped vehicle in a cold start scenario, computed by nonlinear solver IPopt and Algorithm 1. The bottom graph additionally shows the overheating temperature limits and a validation by comparing it with a Motor-CAD simulation. The optimal results are presented by the solid lines, the almost convex problem results are presented by the thin dashed lines and the Motor-CAD validation data is presented by the thick dashed lines. The nonlinear and almost convex solutions are almost indistinguishable.

the iteration of Problem 3, and it yields $x^\star_{\mathrm{CVX,i}}$ at the i^{th} iteration, and Problem 1 which reaches an optimal solution $x^\star_{\mathrm{NL}}$. We remind that Algorithm 1 is defined as Problem 1 where the speed is divided in $[v, \bar{v}]$ and the convex Problem 3 is solved iteratively for the additional external constraint $v = \bar{v}$ satisfied with a defined tolerance.

We note as $x^\star_{\mathrm{CVX}}(\bar{v_1})$ the solution of Problem 3 when $\bar{v} = v_1$ and unique solution for battery-limited scenarios. We can prove Problem 3 is injective by showing that

$$\begin{aligned} &\text{if} \quad v_1 = v_2 \Rightarrow v_1^\star = v_2^\star \\ &\text{if} \quad v_1 \neq v_2 \Rightarrow v_1^\star \neq v_2^\star. \end{aligned}$$

The first condition is satisfied by the strictly convex property of the problem, so we focus on the second condition. If it is not injective, we can reach the same solution for two different $\bar{v}$. We assume that for $\bar{v} = \{v_1 \vee v_2\}$ we reach the set of solutions $x^\star_{\mathrm{CVX}}(\bar{v_1}) = x^\star_{\mathrm{CVX}}(\bar{v_2})$.

Now we consider an active thermal constraint of Problem 3 that is of the form

$$\frac{\mathrm{d}}{\mathrm{d}s}\vartheta_{\mathrm{i}}(s) \cdot c_{\mathrm{i}} \cdot \bar{v}(s) = P_{\mathrm{i}}(s) + \sum_{i,j} k_{\mathrm{i,j}} * \Delta\vartheta_{\mathrm{i,j}}$$

where

$$\begin{aligned} P_i(s) &= x_i(s)^\top Q_i x_i(s), \\ x_i(s) &= \begin{bmatrix} 1 & \omega_{\mathrm{m}}(s) & P_{\mathrm{m}}(s) \end{bmatrix}^\top, \\ P_{\mathrm{m}}(s) &= F_{\mathrm{m}}(s) \cdot \bar{v}(s) \\ \frac{\mathrm{d}}{\mathrm{d}s}E_{\mathrm{kin}}(s) &= F_{\mathrm{m}}(s) - F_{\mathrm{drag}}(s) \quad \text{approx.} \end{aligned}$$

We note that in the thermal constraint the left hand side is proportional to $\bar{v}$. The power is also proportional to $\bar{v}$ but it also increases with $v(s)$ through the kinetic energy and the drag force.

Since we supposed $x^\star_{\mathrm{CVX}}(\bar{v_1}) = x^\star_{\mathrm{CVX}}(\bar{v_2})$, the speeds $v^\star(s)$ are the same, the drag forces and kinetic energies are the same and also the motor forces. $x_i(s)$ is linearly dependent on $\bar{v}$ and we can rewrite it as

$$y_i(s) = \frac{x_i(s)}{\bar{v}} = \begin{bmatrix} \frac{\mathrm{d}t}{\mathrm{d}s}(s) & \gamma(s) \cdot \gamma_{\mathrm{fd}}/r_w & F_{\mathrm{m}}(s) \end{bmatrix}^\top. \tag{27}$$

We rewrite the thermal constraint using the optimal trajectories and it becomes

$$\begin{aligned} \frac{\mathrm{d}}{\mathrm{d}s}\vartheta^\star_{\mathrm{i}}(s) \cdot c_{\mathrm{i}} \cdot \bar{v}(s) &= \bar{v}^2(s) \cdot y_i^{\star\top} Q_i y_i^\star + \sum_{i,j} k_{\mathrm{i,j}} * \Delta\vartheta^\star_{\mathrm{i,j}} \\ b \cdot \bar{v} &= \bar{v}^2 \cdot a + c \end{aligned} \tag{28}$$

where a, b, c are all constants. Now we hypothesize $v_1 \neq v_2$. The constraint has to be satisfied for $\bar{v} = \{v_1 \vee v_2\}$ with $v_1 \neq v_2$. With $\Delta v = v_2 - v_1$ we write

$$\begin{aligned} b \cdot (v_1) &= (v_1)^2 \cdot a + c \\ b \cdot (v_1 + \Delta v) &= (v_1 + \Delta v)^2 \cdot a + c \end{aligned}$$

We expand the second equation and use the first equation to cancel some addends. After some algebraic steps we arrive at a second order polynomial with the following solutions.

$$\Delta v = 0 \quad \text{and} \quad \Delta v = \frac{b}{a} - 2v_1$$

We substitute Δv and obtain

$$v_2 = v_1 \quad \text{and} \quad v_2 = \frac{b}{a} - v_1.$$

In the second solution, a represents the power loss which is always positive, v_1 is the constant speed which is also always positive, and b is the energy absorbed by the node in space domain $\frac{\mathrm{d}}{\mathrm{d}s}\vartheta_{\mathrm{i}}(s) \cdot c_{\mathrm{i}} \in \mathbb{R}^{\mathrm{N_t}}$. $\vartheta_{\mathrm{i}}(s)$ is generally not monotonically increasing, therefore

$$\exists\ \tau \in \{[1, N_t] \cap \mathbb{N}\} \mid \frac{\mathrm{d}}{\mathrm{d}s}\vartheta_{\mathrm{i}}(\tau) \leq 0 \Rightarrow \exists\ v_2 \leq 0 \Rightarrow \nexists.$$

We can conclude that

$$v_2^\star = v_1^\star \iff \bar{v} = \{v_1 \vee v_2\} \mid v_1 = v_2$$

This proves that if $v_1 \neq v_2 \Rightarrow v_1^\star \neq v_2^\star$, therefore Problem 3 is injective in the speed.

Now we study how this property effects the convergence of Algorithm 1. We suppose that the nonlinear solution $x^\star_{\mathrm{NL}}$ is known and Algorithm 1 reached at the i^{th}

$$x^\star_{\mathrm{CVX,i}}(\bar{v}^\star_{\mathrm{CVX,(i-1)}}) = x^\star_{\mathrm{NL}}$$

where $v^\star_{\mathrm{CVX,(i-1)}}$ is part of the optimal solution at the $i-1$ iteration. We know that $x^\star_{\mathrm{CVX}}$ is uniquely identified by a $\bar{v}$ because Problem 3 is injective.

Since $x^\star_{\mathrm{NL}} = x^\star_{\mathrm{CVX,i}}$ we know that they both satisfy the thermal constraints. In doing so, the difference is that for NL $\bar{v}$ is the optimization variable v and it assumes the value

of $v^\star_{\mathrm{NL}}$, while for CVX $\bar{v} = v^\star_{\mathrm{CVX},(\mathrm{i}-1)}$. We can prove that $v^\star_{\mathrm{CVX},(\mathrm{i}-1)} = v^\star_{\mathrm{NL}}$ using the same proof starting from Eq. [28]. Finally, we wish to recall that Problem 3 has a unique solution and it is injective. Therefore,

$$x^\star_{\mathrm{CVX},(\mathrm{i}-1)}(\bar{v}^\star_{\mathrm{CVX},(\mathrm{i}-2)}) = x^\star_{\mathrm{NL}},$$

since $v^\star_{\mathrm{CVX},(\mathrm{i}-1)} = v^\star_{\mathrm{NL}}$ and $v^\star_{\mathrm{CVX},(\mathrm{i}-1)}$ is part of the set of unique solutions $x^\star_{\mathrm{CVX},(\mathrm{i}-1)}$.

To conclude, Algorithm 1 reaches the nonlinear solution only by starting from the nonlinear solution. This could be possible with an infinite number of iterations. This also proves that instead of abruptly reaching a fixed point, Algorithm 1 gradually converges to it, which is in line with our results.

To theoretically study the convergency of this method in more detail we suggest to investigate block coordinate methods. It should be noted that the lack of the constraint $v = \bar{v}$ hides some of the problem dynamics to the convex approach. If a block coordinate method is used, we suggest treating the speed as a unique optimization variable. The literature of these methods provides extensive documentation of convergence rates and optimality discussions.

REFERENCES

[1] T. Sedlacek, D. Odenthal, and D. Wollherr, "Minimum-time optimal control for battery electric vehicles with four wheel-independt drives considering electrical overloading," *Vehicle System Dynamics*, 2020.

[2] T. Herrmann, F. Passigato, J. Betz, and M. Lienkamp, "Minimum race-time planning-strategy for an autonomous electric racecar," in *Proc. IEEE Int. Conf. on Intelligent Transportation Systems*, 2020.

[3] X. Liu, A. Fotouhi, and D. Auger, "Optimal energy management for formula-e cars with regulatory limits and thermal constraints," *Applied Energies*, vol. 279, 2020.

[4] S. Ebbesen, M. Salazar, P. Elbert, C. Bussi, and C. H. Onder, "Time-optimal control strategies for a hybrid electric race car," *IEEE Transactions on Control Systems Technology*, vol. 26, no. 1, pp. 233–247, 2018.

[5] O. Borsboom, C. A. Fahdzyana, T. Hofman, and M. Salazar, "A convex optimization framework for minimum lap time design and control of electric race cars," *IEEE Transactions on Vehicular Technology*, 2020, submitted.

[6] M. Salazar, P. Elbert, S. Ebbesen, C. Bussi, and C. H. Onder, "Time-optimal control policy for a hybrid electric race car," *IEEE Transactions on Control Systems Technology*, vol. 25, no. 6, pp. 1921–1934, 2017.

[7] M. Salazar, P. Duhr, C. Balerna, L. Arzilli, and C. H. Onder, "Minimum lap time control of hybrid electric race cars in qualifying scenarios," *IEEE Transactions on Vehicular Technology*, vol. 68, no. 8, pp. 7296–7308, 2019.

[8] P. Duhr, G. Christodoulou, C. Balerna, M. Salazar, A. Cerofolini, and C. H. Onder, "Time-optimal gearshift and energy management strategies for a hybrid electric race car," *Applied Energy*, vol. 282, no. 115980, 2020.

[9] A. Boglietti, A. Cavagnino, D. Staton, M. Shanel, M. Mueller, and C. Mejuto, "Evolution and modern approaches for thermal analysis of electrical machines," *IEEE Transactions on Industrial Electronics*, vol. 56, no. 3, pp. 871–882, 2009.

[10] S. Kapatral, O. Iqbal, and P. Modi, "Numerical modeling of direct-oil-cooled electric motor for effective thermal management," in *SAE World Congress*, 2020.

[11] J. Dong, Y. Huang, L. Jin, H. Lin, and H. Yang, "Thermal optimization of a high-speed permanent magnet motor," *IEEE Transactions on Magnetics*, vol. 50, no. 2, pp. 749–752, 2014.

[12] G. Demetriades, H. Zelaya de la Parra, E. Andersson, and H. Olsson, "A real-time thermal model of a permanent-magnet synchronous motor," *IEEE Transactions on Power Electronics*, vol. 25, no. 2, pp. 463–474, 2010.

[13] C. Sciascera, P. Giangrande, L. Papini, C. Gerada, and M. Galea, "Analytical thermal model for fast stator winding temperature prediction," *IEEE Transactions on Industrial Electronics*, vol. 64, no. 8, pp. 6116–6126, 2017.

[14] O. Borsboom, C. A. Fahdzyana, M. Salazar, and T. Hofman, "Time-optimal control strategies for electric race cars for different transmission technologies," in *IEEE Vehicle Power and Propulsion Conference*, 2020, in press.

[15] Ansys Motor-CAD. ANSYS, Inc. Available at https://www.ansys.com/products/electronics/ansys-motor-cad.

[16] A. Locatello, M. Konda, O. Borsboom, T. Hofman, and M. Salazar, "Time-optimal control of electric race cars under thermal constraints," in *European Control Conference*, 2021, under review.

[17] D. Rotenberg, A. Vahidi, and I. Kolmanovsky, "Ultracapacitor assisted powertrainds: Modeling, control, sizing, and the impact on fuel economy," *IEEE Transactions on Control Systems Technology*, vol. 19, no. 3, pp. 576–589, 2011.

[18] V. Madonna, A. Walker, P. Giangrande, G. Serra, C. Gerada, and M. Galea, "Improved thermal management and analysis for stator end-windings of electrical machines," *IEEE Transactions on Industrial Electronics*, vol. 66, no. 7, pp. 5057–5069, 2018.

[19] F. J. R. Verbruggen, M. Salazar, M. Pavone, and T. Hofman, "Joint design and control of electric vehicle propulsion systems," in *European Control Conference*, 2020.

[20] J. Löfberg, "YALMIP : A toolbox for modeling and optimization in MATLAB," in *IEEE Int. Symp. on Computer Aided Control Systems Design*, 2004.

[21] A. Domahidi, E. Chu, and S. Boyd, "Ecos: An socp solver for embedded systems," in *European Control Conference*, 2013.

[22] A. Wachter and L. T. Biegler, "On the implementation of an interior-point filter line-search algorithm for large-scale nonlinear programming," *Mathematical Programming*, vol. 106, no. 1, pp. 25–57, 2006.

[23] J. A. E. Andersson, J. Gillis, G. Horn, J. B. Rawlings, and M. Diehl, "Casadi – a software framework for nonlinear optimization and optimal control," *Mathematical Programming Computation*, vol. 11, no. 1, pp. 1–36, 2019.

[24] Y. X. and W. Y., "A globally convergent algorithm for nonconvex optimization based on block coordinate update," *Journal of Scientific Computing*, vol. 72, pp. 700–734, 2017.